MATERIALS CHEMISTRY
FRONTIERS

RESEARCH ARTICLE

View Article Online
View Journal | View Issue

Cite this: *Mater. Chem. Front.*, 2024, **8**, 2866

A heterocyclic strategy for regulating the proportion of type I and type II photodynamic therapy†

Hui Tang,[ab] Ning Ma,[ab] Xiaochun Liu,[ab] Shiyu Wu,[ab] Hairong Li,[ab] Kangyao Chen,[ab] Yitong Jiang,[ab] Yahui Zhang, *[ab] Zhouyu Wang*[ab] and Xiaoqi Yu [ac]

Received 14th May 2024,
Accepted 3rd July 2024

DOI: 10.1039/d4qm00399c

rsc.li/frontiers-materials

Type I photosensitizers (PSs) used in photodynamic therapy (PDT) offer advanced capabilities because they can generate cytotoxic reactive oxygen species (ROS) through electron transfer, even in hypoxic environments. However, this process is more challenging compared to the type II process *via* energy transfer. Herein, we present a facile and effective strategy to regulate the proportion of the two types of PSs by converting type II PSs to type I PSs through the introduction of heterocyclic rings. Three tetraphenyl-1,3-butadiene (TPB) derivatives were synthesized, each incorporating a different "bridge" molecule: benzene (TPP), thiophene (TPS), and furan (TPO), forming typical D–A structures. Compared with TPP, the electron-rich heterocyclic derivatives TPS and TPO produce more ROS, with type I ROS accounting for a higher proportion. This enhancement is attributed to the lone pair of electrons in the heterocyclic rings, which enhances the intersystem crossing and electron transfer. Systematic and detailed experimental and theoretical calculations prove our findings: $(\text{yield of ROS})_{TPO} > (\text{yield of ROS})_{TPS} > (\text{yield of ROS})_{TPP}$, and $(\text{proportion of type I ROS})_{TPO} > (\text{proportion of type I ROS})_{TPS} > (\text{proportion of type I ROS})_{TPP}$. This strategy not only provides a pathway for developing new PSs, but also lays the foundation for designing pure type I PSs.

Introduction

Photodynamic therapy (PDT) has garnered significant attention in oncology and, to some extent, has served as a kind of role model for other therapeutic areas due to its minimal invasiveness, high spatiotemporal selectivity, low systemic side effects, and negligible drug resistance.[1–4] PDT involves the use of light-excited photosensitizers (PSs) to generate cytotoxic reactive oxygen species (ROS).[5–8] The mechanism of PDT has been progressively elucidated: PSs reach an excited triplet state (^{3}PS*) upon light irradiation, followed by the sensitization of molecular oxygen (O_2).[9–11] There are two pathways for ROS generation: excitation energy transfer (EET) and electron transfer (ET). EET leads to the production of singlet oxygen ($^1O_2$), a process known as type II PDT.[12–14] Unfortunately, type II PSs are highly O_2-dependent, limiting their therapeutic efficacy against hypoxic solid tumors (oxygen pressure < 5 mm Hg).[15–17] On the other hand, type I PDT involves an ET reaction between adjacent biological substrates and ^{3}PS*. The ROS produced by type I PSs include superoxide anions ($O_2^{-\bullet}$), hydrogen peroxide (H_2O_2), and hydroxyl radicals ($OH^\bullet$) sequentially. Type I PDT, due to its continuous oxygen cycle in the ET reaction, is considered one of the most effective strategies to combat the effects of hypoxia in solid tumors.[18–21] Up to now, a variety of PSs have been approved and successfully applied.[22] However, type I PSs are less frequently reported compared to type II PSs, mainly because the cascade ET reactions in type I PDT are less efficient and often overshadowed by EET.[23–25] In many PDT processes, both type I and type II PSs coexist.[26–28] Therefore, developing a facile and effective strategy to regulate the proportion of type I and type II PSs is crucial. This approach could further increase the proportion of type I PSs and facilitate the design of pure type I PSs.

The ET reaction is a key factor for the formation of type I PDT, therefore, improving the electron transfer capability between PSs and substrates using electron-rich structures is a widely acknowledged and studied approach.[29–32] Some PSs with a dominant type I pathway have demonstrated promising results. For instance, Song *et al.* opened a new strategy by employing bovine serum albumin (BSA) as an "electron

[a] *Department of Chemistry, School of Science, Xihua University, Chengdu, 610039, China. E-mail: yahuizhang@mail.xhu.edu.cn, zhouyuwang@mail.xhu.edu.cn*
[b] *Sichuan Engineering Research Center for Molecular Targeted Diagnostic & Therapeutic Drugs, Chengdu, 610039, China*
[c] *Key Laboratory of Green Chemistry and Technology of Ministry of Education, College of Chemistry, Sichuan University, Chengdu 61064, China*

† Electronic supplementary information (ESI) available. See DOI: https://doi.org/10.1039/d4qm00399c

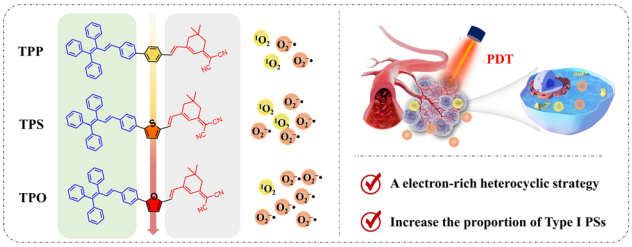

Fig. 1 Chemical structure of TPP, TPS, and TPO and schematic diagram of PDT processes.

reservoir'' to continuously provide electrons, thereby generating more $O_2^{-\bullet}$.[33] Tang *et al.* proposed a strategy involving electron-rich anion–π^+ aggregation-induced emission (AIE) active luminogens to boost type I ROS generation.[34]

Herein, we constructed a heterocyclic strategy to increase the proportion of type I PSs through electron-rich engineering. Three organic PSs, TPP, TPS, and TPO, based on tetraphenyl-1,3-butadiene (TPB) were designed and synthesized, each capable of activating both type I and type II mechanisms upon white-light irradiation. As shown in Fig. 1, three PSs exhibited typical D–A structures, derived from distinct building blocks: (1) TPB, serving as AIE-active donors (D) to suppress nonradiative internal conversion in the aggregated state; (2) the ''bridge'' thiophene and furan, acting as heterocyclic rings to create electron-rich conditions compared to benzene; (3) 2-(3,5,5-trimethylcyclohex-2-en-1-ylidene)malononitrile, acting as an electron acceptor (A). The D–A structure facilitated further a redshift in the emission wavelength, enabling these PSs to reach the near infrared I (NIR-I) region. The presence of electron-rich heterocyclic rings effectively increased the proportion of type I PSs. Both experimental and theoretical results supported our proposed heterocyclic strategy. The significant proportion of type I ROS ($O_2^{-\bullet}$ and $OH^\bullet$) enabled TPO to demonstrate excellent *in vitro* and *in vivo* PDT efficiency.

Results and discussion

Our group has dedicated efforts to exploring the photophysical properties and applications of multiphenyl-substituted 1,3-butadiene and its derivatives. Among these, TPB stands out as a promising luminous core due to its simple synthesis, ease of modification, and AIE properties.[35,36] To develop type I PSs with NIR emission capabilities, TPB was selected as the electron donor (D), and 2-(3,5,5-trimethylcyclohex-2-en-1-ylidene)-malononitrile served as the electron acceptor (A). These components were linked by a benzene ring (heterocyclic ring) serving as a ''bridge''. This typical D–A structure effectively redshifts the emission wavelength, boosts intersystem crossing (ISC), and promotes ROS generation.[37–40] Meanwhile, the lone pair electrons of the heterocyclic ring further increase the ISC, facilitating electron transfer and leading to increased type I ROS production.[41–44] The synthesis route for TPP, TPS, and TPO was illustrated in Fig. S1 (ESI†) and the intermediates and the three products were confirmed using H/C NMR and mass spectrometry, as depicted in Fig. S2–S22 (ESI†).

Fig. 2a and Table 1 illustrated that the maximal absorption peak of TPP in THF was located at 430 nm. As expected, upon substituting the ''bridge'' with furan and thiophene, the maximal absorption peaks undergo a redshift to 478 nm and 496 nm, respectively. Furthermore, the photoluminescence (PL) spectra of the solutions also showed the same redshift result (Fig. 2b). In the solid state, the emission peaks of the heterocyclic rings, TPS (723 nm) and TPO (762 nm), were longer than those of benzene, TPP (709 nm), with the wavelength tail extending to 850 nm, covering the NIR-I region (Fig. S23 (ESI†) and Table 1). Moreover, TPP exhibited typical AIE properties, with strong emission observed in the aggregated state (Fig. S24, ESI†). The fluorescence quantum yield (Φ_f) of the solid was 8.89 times higher than that of the solution.

The fluorescent indicator 2′,7′-dichlorodihydrofluorescein diacetate (H_2DCF-DA), dihydrorhodamine 123 (DHR123), and 9,10-anthracenediylbis(methylene)-dimalonic acid (ABDA) were selected as indicators to evaluate total ROS production, type I ROS ($O_2^{-\bullet}$), and type II ($^1O_2$), respectively. (i) The sharp increase in fluorescence of DCFH confirmed that all three PSs could produce ROS, with the order of (yield of ROS)$_{TPO}$ > (yield of ROS)$_{TPS}$ > (yield of ROS)$_{TPP}$. As shown in Fig. 2c, d and Fig. S25 and S26 (ESI†), the fluorescence intensity of DCFH increased 22.49-fold for TPP, 36.95-fold for TPS, and 85.83-fold for TPO, respectively. (ii) The fluorescence growth at 525 nm of DHR123 was 9.8-fold for TPP, 104.81-fold for TPS, and 136.41-fold for TPO, confirming the production of type I ROS. The proportion of type I ROS followed the order (proportion of type I ROS)$_{TPO}$ > (proportion of type I ROS)$_{TPS}$ > (proportion of type I ROS)$_{TPP}$, as shown in Fig. 2e and Fig. S27 and S28 (ESI†). (iii) The decreased absorption intensity of ABDA indicated the yield of $^1O_2$, indirectly confirming the above conclusion (Fig. 2e and Fig. S29 and S30, ESI†). The $O_2^{-\bullet}$ produced by type I PDT then reacted to form $OH^\bullet$,[34,45] further confirmed using electron paramagnetic resonance (EPR) spectroscopy. The characteristic paramagnetic adducts matching the $OH^\bullet$ signal (1 : 2 : 2 : 1) and $^1O_2$ (1 : 1 : 1) were shown in Fig. 2f–h.

To further explain the effect of heterocycles, especially the furan ''bridge'', on the total amount and variety of ROS, theoretical studies and electrochemical experiments were conducted. The highest occupied molecular orbital (HOMO) and lowest unoccupied molecular orbital (LUMO) of TPP, TPS, and TPO were analyzed and separated (Fig. S31, ESI†). Meanwhile, as shown in Fig. 2i, the energy gap (ΔE_{S1-T3}) of TPP, TPS, and TPO was determined to be 0.11, 0.11, and 0.02 eV, respectively. This finding indicated that the electron-rich structure of furan promoted ISC, thus increasing the production of ROS. Based on these experimental phenomena, it can be reasonably speculated that heterocycles contributed to the formation of $O_2^{-\bullet}$. Type I PSs have lower reduction potentials due to their strong electron-accepting nature.[46,47] Therefore, electrochemical experiments were carried out using cyclic voltammetry (CV), as shown in Fig. S32 (ESI†). TPP, TPO, and TPS all exhibited obvious reduction peaks, with a slight enhancement in the low

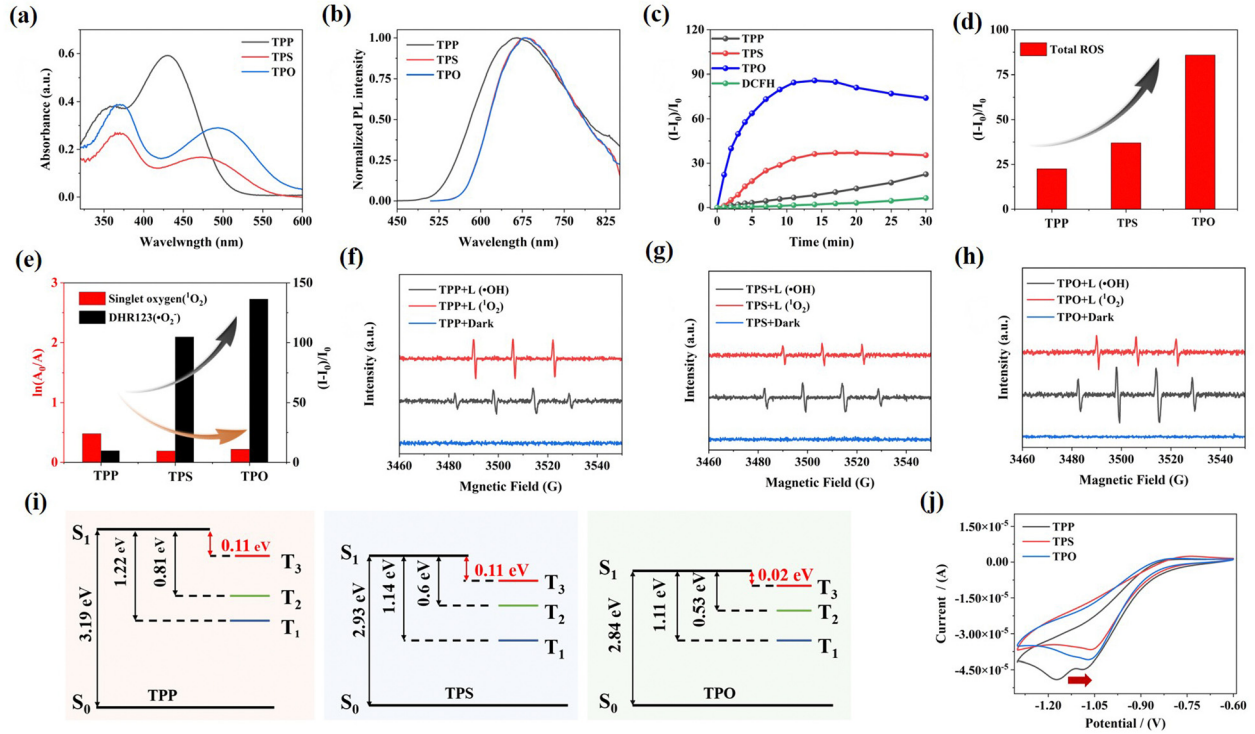

Fig. 2 (a) UV–vis absorption spectra and (b) Normalized PL of TPP, TPS, and TPO in THF. (c) Fluorescence intensity net change $[(I - I_0)/I_0]$ at 532 nm (d) Plots of relative integration fluorescence intensity for the DCFH indicator with TPP, TPS, and TPO upon white light irradiation (2 mW cm^{-2}), [DCFH] = 40 μM. (e) Plots of relative integration fluorescence intensity for the DHR123 and ABDA indicators with TPP, TPS, and TPO upon white light irradiation (2 mW cm^{-2}), [DHR123] = [ABDA] = 40 μM. [TPP] = [TPS] = [TPO] = 1.0 × 10^{-5} mol L^{-1}. EPR spectroscopy of (f) TPP, (g) TPS, and (h) TPO. (i) Relative energy levels of TPP, TPS, and TPO calculated by TD-DFT. (j) The 90th cyclic voltammogram of TPP, TPS, and TPO in DCM with 0.1 M $(n\text{-Bu})_4N^+PF_6^-$ as the supporting electrolyte, Ag/Ag^+ as the reference electrode, a glassy-carbon electrode as the working electrode, and a Pt wire as the counter electrode; scan rate, 50 mV s^{-1}.

Table 1 Photophysical Properties of TPP, TPS, and TPO

		λ_{em} (nm)			Φ_f				
	λ_{abs} (nm)	In THF	Solid	λ_{em} (nm) (NPs)	0%[a]	90%[a]	Solid	ε (10^4 M^{-1} cm^{-1})	Φ_{probe}[b]
TPP	430	660	709	653	1.60	12.79	14.22	4.97	0.2
TPS	478	680	723	707	1.08	1.68	2.48	4.40	0.1
TPO	496	680	762	722	2.87	1.69	2.48	4.32	0.1

[a] Water fraction of THF/H_2O mixture. [b] The yield of $^1O_2$ of probe.

ground state reduction potential $E_{red}(PS/PS^{-\bullet})$ sufficiently lower than −0.33 V ($E_{red}(O_2/O_2^{-\bullet})$ = −0.33 V). Compared to benzene, the anodic shift observed in the heterocyclic "bridge" indicated that TPO had a greater propensity to accept electrons (Fig. 2j).

The uniformity in size, water solubility, and biocompatibility of PSs have significant influence on their effectiveness *in vitro*/*vivo* imaging and PDT.[48–50] TPP, TPS, and TPO were prepared into nanoparticles (NPs) with F127 *via* a "top-down" approach, and their photophysical and PDT properties were systematically studied. As shown in Fig. 3a and Fig. S33 (ESI†), the sizes of the NPs were measured to be 40.12, 39.15, and 38.12 nm, respectively, using dynamic light scattering. These sizes remained relatively constant over 7 days, indicating good stability of the NPs. Moreover, the prepared NPs retained excellent photophysical properties (Fig. S34, ESI†). Compared to the solid state, the emission wavelengths of three nanoparticles exhibited a slight blue shift, but remained at 653 nm (TPP NPs), 707 nm (TPS NPs), and 722 nm (TPO NPs), respectively, as shown in Fig. 3b and Table 1. After coating with F127, the ROS production capability of the three PSs was altered, but TPO NPs remained the most effective in both total ROS and the proportion of type I ROS. Fig. 3c demonstrated that the ROS yield of TPO NPs was 2.08 and 1.98 times higher than that of TPP and TPS NPs, respectively. Additionally, DHR123 and ABDA experiments confirmed that the heterocyclic "bridge" in TPS and TPO NPs led to increased production of type I ROS (Fig. 3d and Fig. S35–S38, ESI†).

The prepared TPO NPs were subsequently applied in cell imaging and *in vitro* PDT. As shown in Fig. 4a, a methyl

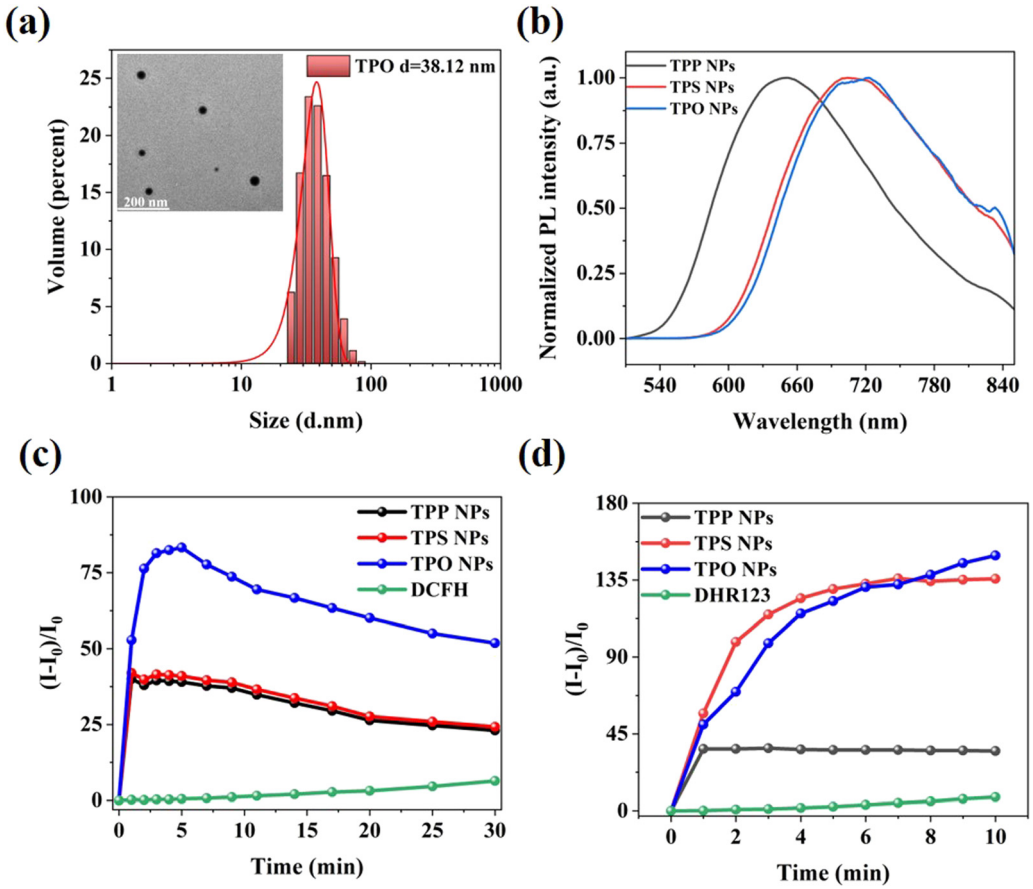

Fig. 3 (a) Dynamic laser scattering size and TEM image (inset) of TPO NPs. Scale bar: 200 nm. (b) Normalized PL of TPP, TPS, and TPO NPs. (c) Fluorescence intensity net change $[(I - I_0)/I_0]$ at 532 nm for the DCFH indicator with TPO NPs upon white light irradiation (2 mW cm^{-2}). (d) Fluorescence intensity net change $[(I - I_0)/I_0]$ at 525 nm for the DHR123 indicator with TPP, TPS, and TPO NPs upon white light irradiation (2 mW cm^{-2}), [DCFH] = 40 μM, [DHR123] = 40 μM, [TPP NPs] = [TPS NPs] = [TPO NPs] = 1.0×10^{-5} mol L^{-1}.

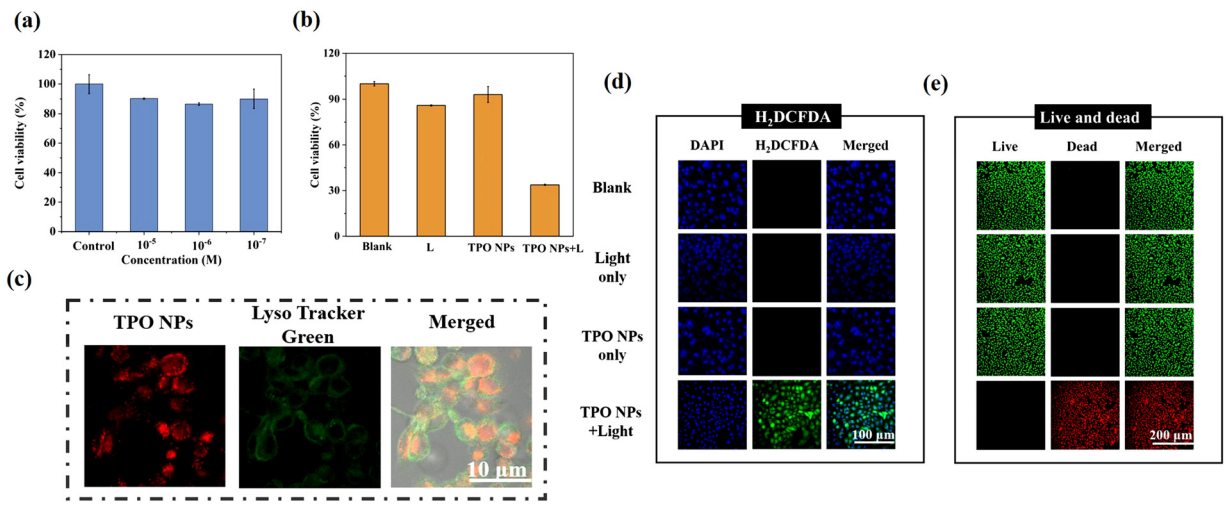

Fig. 4 Cell survival rate (a) without and (b) with TPO NPs upon white light irradiation. (c) Confocal microscopy images of LysoTracker (lysosome maker), TPS NPs and merge. (d) Fluorescence images by CLSM of 4T1 cells stained with H_2DCFDA. (e) Fluorescence images by CLSM of 4T1 cells stained with Calcein-AM/PI. [TPS NPs] = 1.0×10^{-5} mol L^{-1}; white light irradiation (5 mW cm^{-2}, 10 min).

thiazolyltetrazolium (MTT) assay displayed that even at a concentration of 1×10^{-5} mol L^{-1}, TPO NPs exhibited a high cell survival rate of 90%, indicating negligible dark cytotoxic effects. However, ~70% of the 4T1 cells were killed when

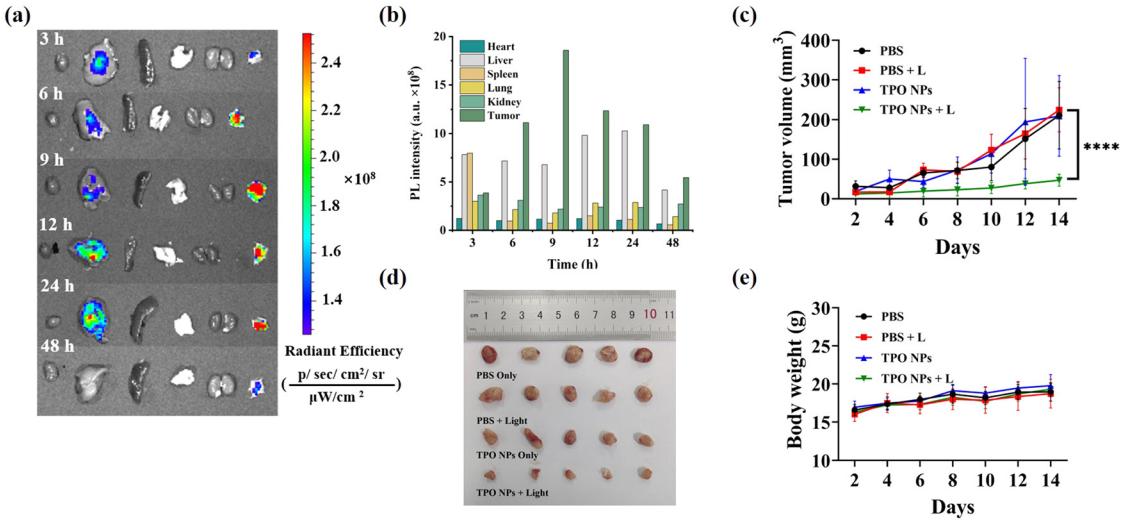

Fig. 5 (a) *Ex vivo* fluorescence images of major organs and tumors following i.v. injection of TPO NPs. (b) Quantitative *ex vivo* fluorescence intensity of major organs and tumors after i.v. injection 9 h. (c) Tumor volume growth curves of mice at different times after treatment. (d) Representative tumor images of mice following different treatments. (e) Body weight measurements of mice in different groups. Data are presented as the average ± standard deviation (n = 5); statistical significance: ****$P < 0.0001$ [TPS NPs] = 1.0×10^{-5} mol L^{-1}; white light irradiation (200 mW cm^{-2}, 10 min).

treated with TPO NPs under white-light irradiation of 5 mW cm^{-2} for 10 min (Fig. 4b). Significant fluorescence signals from TPO NPs were observed over the incubation period, evidencing their accumulation within the 4T1 cells and laying a foundation for *in vivo* imaging. In H_2DCFDA and live/dead cell staining assays, different fluorescence colors visualized the PDT results. No ROS signals were detected in the Blank group, Light-only group and TPO NPs-only group, with only blue fluorescence (representing the nucleus) observed. However, in the TPO NPs + Light group, numerous green signals representing generated ROS were evident, demonstrating the PDT effect (Fig. 4d). Similarly, a substantial number of red fluorescent signals indicative of dead cells appeared in the TPO NPs + Light group, confirming the excellent PDT efficacy of TPO NPs *in vitro* as shown in Fig. 4e.

Encouraged by the promising results of *in vitro* PDT, we applied TPO NPs for imaging and therapeutic purpose *in vivo*. The *ex vivo* biodistribution of tumor-bearing mice was evaluated at different time points following intravenous injection of TPO NPs using the IVIS instrument. As shown in Fig. 5a and b, a significant fluorescence signal was detected at the tumor site after 6 h. The signal intensity reached its highest at 9 hours, with an intensity reaching 2.7 times that of the liver area, indicating efficient tumor accumulation. Notably, the fluorescence signal became hardly visible after 48 hours, indicating favorable biological metabolic capacity and biosafety of TPO NPs. Subsequently, to evaluate the actual PDT effect of TPO NPs *in vivo*, 4T1 tumor-bearing mice with primary tumor volumes of approximately 100 mm^3 were randomly divided into four groups (5 mice in per group), including PBS Only, PBS + Light, TPO NPs only, and TPO NPs + Light (detailed procedure provided in SI). After 9 hours of tail vein injection, the tumors of mice in each group were continuously irradiated with white light (200 mW cm^{-2}) for 10 min. Following the respective treatments, tumor size and body weight of the mice were monitored for 14 days, with the results shown in Fig. 5c–e. Tumors in the first three groups (PBS Only, PBS + Light, TPO NPs only) showed significant further deterioration, demonstrating that TPO NPs or light alone could not suppress the tumor growth. However, tumors in the treatment group were significantly suppressed, as evidenced by tumor size reduction (Fig. 5c) and photographic evidence (Fig. 5d). All the mice showed normal body weight changes during the entire PDT treatment (Fig. 5e), demonstrating the good biosafety of our TPO NPs. The biochemical test results of all mice remained within the normal range (Fig. S39, ESI†). Furthermore, H&E staining results showed no obvious lesions in the major tissues and organs of the mice (Fig. S40, ESI†), thus confirming the safety of TPO PSs as an antitumor therapy.

Conclusions

In summary, a series of TPB derivatives (TPP, TPS, and TPO) featuring a typical D–A structure were synthesized, emitting light in the NIR-I region. By incorporating heterocyclic "bridges", we developed a strategy to modulate the proportion of type I ROS. Both theoretical and experimental results revealed that TPO, with a furan heterocyclic ring as the "bridges", exhibited enhanced ISC, a smaller ΔE_{st}, and an anodic shift in reduction peaks, thus achieving a high ROS yield and a high proportion of type I ROS. Specifically, the order of ROS yield was $(\text{yield of ROS})_{TPO} > (\text{yield of ROS})_{TPS} > (\text{yield of ROS})_{TPP}$, and the order of proportion of type I ROS was TPO > TPS > TPP. As such, this facile and accurate heterocyclic strategy provides a valuable model for designing PSs with a high proportion type I PSs or even pure type I PSs of PDT applications.

Data availability

Experimental details and photophysical properties data for the photosensitizers have been included as part of the ESI.†

Conflicts of interest

The authors declare no conflict of interest.

Acknowledgements

This work was financially supported by the Sichuan Science and Technology Program (2023NSFSC1977, 2023NSFSC0637), National Key R&D Program of China (2023YFB3812402, 2023YFB3812400) and Opening Project of the Key Laboratory of Green Catalysis of Higher Education Institutes of Sichuan (LYJ2304).

References

1 K. X. Teng, L. Y. Niu and Q. Z. Yang, Supramolecular Photosensitizer Enables Oxygen-Independent Generation of Hydroxyl Radicals for Photodynamic Therapy, *J. Am. Chem. Soc.*, 2023, **145**, 4081–4087.

2 Y. Huang, F. Qiu, R. J. Chen, D. Y. Yan and X. Y. Zhu, Fluorescence resonance energy transfer-based drug delivery systems for enhanced photodynamic therapy, *J. Mater. Chem. B*, 2020, **8**, 3772–3788.

3 X. S. Li, S. Kolemen, J. Yoon and E. U. Akkaya, Activatable Photosensitizers: Agents for Selective Photodynamic Therapy, *Adv. Funct. Mater.*, 2017, **12**, 26982–26990.

4 H. T. Feng, Y. Y. Li, X. C. Duan, X. X. Wang, C. X. Qi, J. W. Y. Lam, D. Ding and B. Z. Tang, Substitution Activated Precise Phototheranostics through Supramolecular Assembly of AIEgen and Calixarene, *J. Am. Chem. Soc.*, 2020, **142**, 15966–15974.

5 W. P. Fan, P. Huang and X. Y. Chen, Overcoming the Achilles' heel of photodynamic therapy, *Chem. Soc. Rev.*, 2016, **45**, 6488–6519.

6 P. Agostinis, K. Berg, K. A. Cengel, T. H. Foster, A. W. Girotti, S. O. Gollnick, S. M. Hahn, M. R. Hamblin, A. Juzeniene, D. Kessel, M. Korbelik, J. Moan, P. Mroz, D. Nowis, J. Piette, B. C. Wilson and J. Golab, Photodynamic Therapy of Cancer: An Update, *Ca-Cancer J. Clin.*, 2011, **61**, 250–281.

7 G. Durán-Sampedro, N. Epelde-Elezcano, V. Martínez-Martínez, I. Esnal, J. Bañuelos, I. García-Moreno, A. R. Agarrabeitia, S. de la Moya, A. Tabero, A. Lazaro-Carrillo, A. Villanueva, M. J. Ortiz and I. López-Arbeloa, *Dyes Pigm.*, 2017, **142**, 77–87.

8 M. Y. Yang, T. Yang and C. B. Mao, A versatile fluorescent molecular probe endowed with singlet oxygen generation under white-light photosensitization, *Angew. Chem., Int. Ed.*, 2019, **58**, 14066–14080.

9 B. W. Yang, Y. Chen and J. L. Shi, Reactive Oxygen Species (ROS)-Based Nanomedicine, *Chem. Rev.*, 2019, **119**, 4881–4985.

10 S. S. Lucky, K. C. Soo and Y. Zhang, Nanoparticles in Photodynamic Therapy, *Chem. Rev.*, 2015, **115**, 1990–2042.

11 L. Q. Li, C. Shao, T. Liu, Z. C. Chao, H. L. Chen, F. Xiao, H. M. He, Z. X. Wei, Y. L. Zhu, H. Wang, X. D. Zhang, Y. T. Wen, B. Yang, F. He and L. L. Tian, An NIR-II-Emissive Photosensitizer for Hypoxia-Tolerant Photodynamic Theranostics, *Adv. Mater.*, 2020, **32**(45), 2003471.

12 Y. Y. Wang, Y. C. Liu, H. W. Sun and D. S. Guo, Type I photodynamic therapy by organic-inorganic hybrid materials: From strategies to applications, *Coord. Chem. Rev.*, 2019, **395**, 46–62.

13 S. Kwiatkowski, B. Knap, D. Przystupski, J. Saczko, E. Kedzierska, K. Knap-Czop, J. Kotlinska, O. Michel, K. Kotowski and J. Kulbacka, Photodynamic therapy - mechanisms, photosensitizers and combinations, *Biomed. Pharmacother.*, 2018, **106**, 1098–1107.

14 M. Kolarikova, B. Hosikova, H. Dilenko, K. Barton-Tomankova, L. Valkova, R. Bajgar, L. Malina and H. Kolarova, Photodynamic therapy: Innovative approaches for antibacterial and anticancer treatments, *Med. Res. Rev.*, 2023, **43**, 717–774.

15 M. G. V. Heiden, L. C. Cantley and C. B. Thompson, Understanding the Warburg Effect: The Metabolic Requirements of Cell Proliferation, *Science*, 2009, **324**, 1029–1033.

16 X. Y. Deng, Z. W. Shao and Y. L. Zhao, Solutions to the Drawbacks of Photothermal and Photodynamic Cancer Therapy, *Adv. Sci.*, 2021, **8**(3), 2002504.

17 J. F. Miao, Y. Y. Hu, G. X. Yao, Y. Feng, J. J. Weng, W. Zhao and W. Guo, Mitochondria-Targeted, and Activatable Photosensitizers for Photodynamic Therapy with Real-Time In-Situ Therapeutic Monitoring, *Angew. Chem., Int. Ed.*, 2022, **61**(25), e202201815.

18 X. S. Li, N. Kwon, T. Guo, Z. Liu and J. Yoon, Innovative Strategies for Hypoxic-Tumor Photodynamic Therapy, *Angew. Chem., Int. Ed.*, 2018, **57**, 11522–11531.

19 Y. L. Wan, L. H. Fu, C. Y. Li, J. Lin and P. Huang, Conquering the Hypoxia Limitation for Photodynamic Therapy, *Adv. Mater.*, 2021, **33**(48), 2103978.

20 T. K. Luo, K. Y. Ni, A. Culbert, G. X. Lan, Z. Li, X. M. Jiang, M. Kaufmann and W. B. Lin, Nanoscale Metal-Organic Frameworks Stabilize Bacteriochlorins for Type I and Type II Photodynamic Therapy, *J. Am. Chem. Soc.*, 2020, **142**, 7334–7339.

21 L. Huang, S. J. Zhao, J. S. Wu, L. Yu, N. Singh, K. Yang, M. H. Lan, P. F. Wang and J. S. Kim, Photodynamic therapy for hypoxic tumors: Advances and perspectives, *Coord. Chem. Rev.*, 2021, **438**, 213888.

22 X. H. Yu, M. Lyu, X. P. Ou, W. Q. Liu, X. Yang, X. X. Ma, T. F. Zhang, L. N. Wang, Y. C. Zhang, S. J. Chen, R. T. K. Kwok, Z. Zheng, H. L. Cui, L. T. Cai, P. F. Zhang and B. Z. Tang, AIEgens/Mitochondria Nanohybrids as Bioactive Microwave Sensitizers for Non-Thermal Microwave Cancer Therapy, *Adv. Healthcare Mater.*, 2023, **12**(12), 2202907.

23 H. Chen, S. L. Li, M. Wu, Kenry, Z. M. Huang, C. S. Lee and B. Liu, Membrane-Anchoring Photosensitizer with Aggregation-Induced Emission Characteristics for Combating Multidrug-Resistant Bacteria, *Angew. Chem., Int. Ed.*, 2020, **59**, 632–636.

24 H. Mattila, S. Khorobrykh, V. Havurinne and E. Tyystjärvi, Reactive oxygen species: Reactions and detection from photosynthetic tissues, *J. Photochem. Photobiol., B*, 2015, **152**, 176–214.

25 X. S. Li, D. Y. Lee, J. D. Huang and J. Y. Yoon, Phthalocyanine-Assembled Nanodots as Photosensitizers for Highly Efficient Type I Photoreactions in Photodynamic Therapy, *Angew. Chem., Int. Ed.*, 2018, **57**, 9885–9890.

26 Y. W. Yu, S. Wu, L. Zhang, S. D. Xu, C. H. Dai, S. M. Gan, G. F. Xie, G. X. Feng and B. Z. Tang, Cationization to boost both type I and type II ROS generation for photodynamic therapy, *Biomaterials*, 2022, **280**, 121255.

27 X. Cui, J. F. Zhang, Y. P. Wan, F. Fang, R. Chen, D. Shen, Z. M. Huang, S. Tian, Y. F. Xiao, X. Z. Li, J. Chelora, Y. H. Liu, W. J. Zhang and C. S. Lee, Dual Fenton Catalytic Nanoreactor for Integrative Type-I and Type-II Photodynamic Therapy Against Hypoxic Cancer Cells, *ACS Appl. Bio Mater.*, 2019, **2**, 3854–3860.

28 K. Wang, Z. Zhang, L. Lin, J. Chen, K. Hao, H. Y. Tian and X. S. Chen, Covalent Organic Nanosheets Integrated Heterojunction with Two Strategies to Overcome Hypoxic-Tumor Photodynamic Therapy, *Chem. Mater.*, 2019, **31**, 3313–3323.

29 Y. L. Li, D. Zhang, Y. W. Yu, L. Zhang, L. Li, L. L. Shi, G. X. Feng and B. Z. Tang, A Cascade Strategy Boosting Hydroxyl Radical Generation with Aggregation-Induced Emission Photosensitizers-Albumin Complex for Photodynamic Therapy, *ACS Nano*, 2023, **17**, 16993–17003.

30 K. X. Teng, L. Y. Niu and Q. Z. Yang, A host-guest strategy for converting the photodynamic agents from a singlet oxygen generator to a superoxide radical generator, *Chem. Sci.*, 2022, **13**, 5951–5956.

31 K. Q. Chen, P. He, Z. M. Wang and Z. B. Tang, A Feasible Strategy of Fabricating Type I Photosensitizer for Photodynamic Therapy in Cancer Cells and Pathogens, *ACS Nano*, 2021, **15**, 7735–7743.

32 V. N. Nguyen, S. Qi, S. Kim, N. Kwon, G. Kim, Y. Yim, S. Park and J. Yoon, An Emerging Molecular Design Approach to Heavy-Atom-Free Photosensitizers for Enhanced Photodynamic Therapy under Hypoxia, *J. Am. Chem. Soc.*, 2019, **141**, 16243–16248.

33 W. L. Chen, Z. H. Wang, M. Y. Tian, G. B. Hong, Y. N. Wu, M. Z. Sui, M. M. Chen, J. An, F. L. Song and X. J. Peng, A Feasible Strategy of Fabricating Type I Photosensitizer for Photodynamic Therapy in Cancer Cells and Pathogens Integration of TADF Photosensitizer as ''Electron Pump'' and BSA as ''Electron Reservoir'' for Boosting Type I Photodynamic Therapy, *J. Am. Chem. Soc.*, 2023, **145**, 8130–8140.

34 Q. Wan, R. Y. Zhang, Z. Y. Zhuang, Y. X. Li, Y. H. Huang, Z. M. Wang, W. J. Zhang, J. Q. Hou and B. Z. Tang, Molecular Engineering to Boost AIE-Active Free Radical Photogenerators and Enable High-Performance Photodynamic Therapy under Hypoxia, *Adv. Funct. Mater.*, 2020, **30**(39), 2002057.

35 Y. H. Zhang, H. Y. Xu, W. Q. Xu, C. Zhang, J. B. Shi, B. Tong, Z. X. Cai and Y. P. Dong, Conformational sensitivity of tetraphenyl-1,3-butadiene derivatives with aggregation-induced emission characteristics, *Sci. China: Chem.*, 2019, **62**, 1393–1397.

36 Y. H. Zhang, L. W. Kong, H. L. Mao, X. L. Pan, J. B. Shi, B. Tong and Y. P. Dong, Light/temperature-enhanced emission characteristics of malononitrile-containing hexaphenyl-1,3-butadiene derivatives: the hotter, the brighter, *Mater. Chem. Front.*, 2017, **1**, 2569–2573.

37 Z. R. Xu, Y. H. Jiang, M. Z. Fan, S. Tang, M. X. Liu, W. C. Law, C. B. Yang, M. Ying, M. Z. Ma, B. Q. Dong, K. T. Yong and G. X. Xu, Aggregation-Induced Emission Nanoprobes Working in the NIR-II Region: From Material Design to Fluorescence Imaging and Phototherapy, *Adv. Opt. Mater.*, 2021, **9**(20), 2100859.

38 M. M. Kang, C. C. Zhou, S. M. Wu, B. R. Yu, Z. J. Zhang, N. Song, M. M. S. Lee, W. H. Xu, F. J. Xu, D. Wang, L. Wang and B. Z. Tang, Evaluation of Structure-Function Relationships of Aggregation-Induced Emission Luminogens for Simultaneous Dual Applications of Specific Discrimination and Efficient Photodynamic Killing of Gram-positive Bacteria, *J. Am. Chem. Soc.*, 2019, **141**, 16781–16789.

39 L. L. Huang, X. Wen, J. W. Liu, M. X. Chen, Z. Y. Ma and X. R. Jia, An AIE molecule featuring changeable triplet emission between phosphorescence and delayed fluorescence by an external force, *Mater. Chem. Front.*, 2019, **3**, 2151–2156.

40 Y. L. Xu, Y. Zhang, J. Li, J. S. An, C. L. Li, S. Y. Bai, A. Sharma, G. Z. Deng, J. S. Kim and Y. Sun, NIR-II emissive multifunctional AIEgen with single laser-activated synergistic photodynamic/photothermal therapy of cancers and pathogens, *Biomaterials*, 2020, **259**, 120315.

41 G. Yang, S. B. Lu, C. Li, F. Chen, J. S. Ni, M. L. Zha, Y. X. Li, J. Gao, T. Y. Kang, C. Liu and K. Li, Type I macrophage activator photosensitizer against hypoxic tumors, *Chem. Sci.*, 2021, **12**, 14773–14780.

42 K. K. Wen, H. Tan, Q. Peng, H. Chen, H. Ma, L. Wang, A. D. Peng, Q. Q. Shi, X. D. Cai and H. Huang, Achieving Efficient NIR-II Type-I Photosensitizers for Photodynamic/Photothermal Therapy upon Regulating Chalcogen Elements, *Adv. Mater.*, 2022, **34**(7), 2108146.

43 C. Pan, W. J. Zhao, X. L. Zhao, Z. X. Liu, X. Y. Li, Y. Lyu, X. P. Wu, Z. R. Zhu, W. H. Zhu and Q. Wang, Type I photosensitizer based on AIE chromophore tricyanomethylene-pyridine for photodynamic therapy, *Green Chem. Eng.*, 2023, **4**, 324–330.

44 L. R. Wang, J. Qi, K. Zhang, Z. Y. Zhuang, K. K. Ding, X. Chen, H. Shan, D. Ding, A. J. Qin and B. Z. Tang, Multifunctional nanomicelles constructed by an aggregation and deaggregation strategy for magnetic resonance/NIR II fluorescence imaging-guided type I photodynamic therapy, *Mater. Chem. Front.*, 2023, **7**, 3657–3667.

45 M. L. Li, J. Xia, R. S. Tian, J. Y. Wang, J. L. Fan, J. J. Du, S. Long, X. Z. Song, J. W. Foley and X. J. Peng, J. Near-Infrared Light-Initiated Molecular Superoxide Radical Generator: Rejuvenating Photodynamic Therapy against Hypoxic Tumors, *J. Am. Chem. Soc.*, 2018, **140**, 14851–14859.

46 J. An, S. L. Tang, G. B. Hong, W. L. Chen, M. M. Chen, J. T. Song, Z. L. Li, X. J. Peng, F. L. Song and W. H. Zheng, An unexpected strategy to alleviate hypoxia limitation of photodynamic therapy by biotinylation of photosensitizers, *Nat. Commun.*, 2022, **13**, 2225.
47 Z. Y. Zhuang, J. Dai, M. X. Yu, J. Q. Li, C. Shen, R. Hu, X. D. Lou, Z. J. Zhao and B. Z. Tang, Type I photosensitizers based on phosphindole oxide for photodynamic therapy: apoptosis and autophagy induced by endoplasmic reticulum stress, *Chem. Sci.*, 2020, **11**, 3405–3417.
48 C. Xu, J. S. Huang, Y. Y. Jiang, S. S. He, C. Zhang and K. Y. Pu, Nanoparticles with ultrasound-induced afterglow luminescence for tumour-specific theranostics, *Nat. Biomed. Eng.*, 2023, **7**, 298–312.
49 S. M. Gan, W. B. Wu, G. X. Feng, Z. M. Wang, B. Liu and B. Z. Tang, Size Optimization of Organic Nanoparticles with Aggregation-Induced Emission Characteristics for Improved ROS Generation and Photodynamic Cancer Cell Ablation, *Small*, 2022, **18**(26), 2202242.
50 D. D. Guo, X. Y. Dai, K. W. Liu, Y. H. Liu, J. M. Wu, K. Wang, S. W. Jiang, F. Sun, L. J. Wang, B. Guo, D. Y. Yang, L. Q. Huang and A. Self-Reinforcing Nanoplatform, for Highly Effective Synergistic Targeted Combinatary Calcium-Overload and Photodynamic Therapy of Cancer, *Adv. Healthcare Mater.*, 2023, **12**, 19.